J. Fluid Mech. (1996), *vol.* 323, *pp.* 1–22

Turbulence characteristics of a boundary layer over a swept bump

By D. R. WEBSTER†, D. B. DeGRAAFF AND J. K. EATON
Thermosciences Division, Department of Mechanical Engineering, Stanford University,
Stanford, CA 94305-3030, USA

(Received 16 October 1995 and in revised form 11 March 1996)

The evolution of the turbulent boundary layer over a bump defined by three tangential circular arcs and swept at 45° was examined. The flat-plate boundary layer approaching the swept bump had a momentum thickness Reynolds number of approximately 3800. The ratios of upstream boundary-layer thickness to bump height and convex radius of curvature were 1.5 and 0.06, respectively. The boundary layer was influenced by alternating signs of streamwise pressure gradient, wall curvature, and mean crossflow, which resulted in a complex boundary-layer flow that grew rapidly on the downstream side of the bump. The mean flow profiles deviated significantly from typical logarithmic layer behaviour, but the flow remained attached. The evolution of the Reynolds stress components was explained by the growth of two internal layers triggered by discontinuities in wall curvature near the leading and trailing edges of the bump. The shear stress vector was found to lag the velocity gradient vector, despite the spanwise flow changing direction above the bump. The measurements were compared to the previous results from a two-dimensional bump with the same profile shape and Reynolds number. Contrary to previous studies, the addition of mean crossflow to this complex flow field did not reduce the vertical mixing relative to the turbulent kinetic energy.

1. Introduction

A three-dimensional turbulent boundary layer is a wall-attached shear layer in which the mean flow direction varies with distance from the wall and both wall parallel mean vorticity components are significant. The result is a complex strain rate field that combines the basic component, $\partial u/\partial y$, and an extra strain rate, $\partial w/\partial y$, which both vary with distance from the wall. This is contrasted with two-dimensional turbulent boundary layers, in which the velocity at all distances from the wall is parallel to the inviscid free-stream flow, and only the spanwise mean vorticity is significant. Three-dimensional turbulent boundary layers are the norm in naval, aerospace and other applications, while true two-dimensional turbulent boundary layers are rare except in carefully constructed research facilities.

Recent studies have revealed some common characteristics for three-dimensional turbulent boundary layers (see the review by Johnston & Flack 1994). First, the wall-parallel shear stress vector is not aligned with the strain rate vector (i.e. the vector formed by $\overline{u'v'}$ and $\overline{v'w'}$ does not coincide with the vector formed by $\partial u/\partial y$ and $\partial w/\partial y$). Most studies have observed that the shear stress vector lags the strain rate vector, although some authors have observed the converse situation and it seems to be a

---

† Present address: Department of Aerospace Engineering and Mechanics, University of Minnesota, Minneapolis, MN 55455, USA.

function of flow geometry. This lack of alignment prevents scalar eddy viscosity models from properly predicting three-dimensional turbulent boundary layers. Secondly, and more importantly, the ability of the turbulence to mix momentum and scalar quantities across the boundary layer is reduced by mean flow three-dimensionality. Nearly every three-dimensional turbulent-boundary-layer experiment has shown that the Townsend structure parameter, $A_1 = (\overline{u'v'}^2 + \overline{v'w'}^2)^{1/2}/\overline{q^2}$, is reduced by 20–50% when three-dimensionality is imposed. This has been observed in boundary layers approaching obstacles (Fernholz & Vagt 1981; Anderson & Eaton 1989; Ölçmen & Simpson 1995), on the side walls of curved channels (Schwarz & Bradshaw 1994; Truong & Brunet 1992; Flack & Johnston 1993), approaching a swept step (Johnston 1970; Flack & Johnston 1993), over 'infinite' swept wings (van den Berg *et al.* 1975; Bradshaw & Pontikos 1985; Baskaran, Pontikis & Bradshaw 1990), and on a spinning disk (Littell & Eaton 1994). The direct numerical simulations of Spalart (1988), Coleman, Ferziger & Spalart (1990) and Sendstad & Moin (1992) have shown similar reductions in shear stress and turbulent kinetic energy. The simulations showed that the reduction was due to the spanwise directed mean flow breaking up the streamwise-aligned turbulent flow structure. It is clear from the physical experiments and the numerical simulations that the mechanisms responsible for the production of shear stress deep in the boundary layer are somehow modified and rendered less effective by three dimensionality.

The imposition of three dimensionality has usually been coupled with relatively strong streamwise pressure gradients in previous experiments. Such pressure gradients can also cause reductions in A_1. Control experiments in which the same streamwise pressure gradient is applied to both a two-dimensional and a three-dimensional turbulent boundary layer are not available. The goal of the present work was to develop a three-dimensional turbulent-boundary-layer experiment which had an obvious two-dimensional turbulent-boundary-layer analogue. The geometry chosen was the flow over a surface mounted bump swept at a 45° angle, as illustrated in figure 1. The analogue, of course, is an unswept bump with the same streamwise cross-sectional profile. Webster, DeGraaff & Eaton (1996) report the results from a two-dimensional bump that has the same profile shape and Re_θ as the swept bump discussed here.

The bump was defined by three tangential circular arcs and provided the opportunity to examine the combined effects of surface curvature, streamwise pressure gradient, and mean cross-flow. The boundary layer experiences alternating signs of wall curvature: a short concave region, a longer convex region, another short concave region, and then the downstream flat plate. The flow was also subjected to alternating streamwise pressure gradients: first mildly adverse, then strongly favourable, strongly adverse, and finally mildly favourable. In the strong adverse pressure gradient on the downstream side of the bump the boundary layer grew rapidly but did not separate. Figure 1(*a*) shows a carefully sketched surface streamline to indicate how the flow turned as it passed over the bump: first mildly in the sweep direction, then against the sweep, and then strongly in the sweep direction. The flow relaxed rapidly to the free-stream direction downstream of the bump. Based on the results of previous three-dimensional turbulent-boundary-layer investigations, the spanwise mean flow was expected to alter the turbulent characteristics significantly.

The results of Baskaran, Pontikis & Bradshaw (1990) are of particular relevance to the current investigation, since the combined effects of three-dimensionality and wall curvature were examined. They concluded that the important three-dimensional effects were essentially unchanged by mild longitudinal convex curvature. Another relevant experiment was performed by Özcan (1988) who examined the flow over a 45° swept

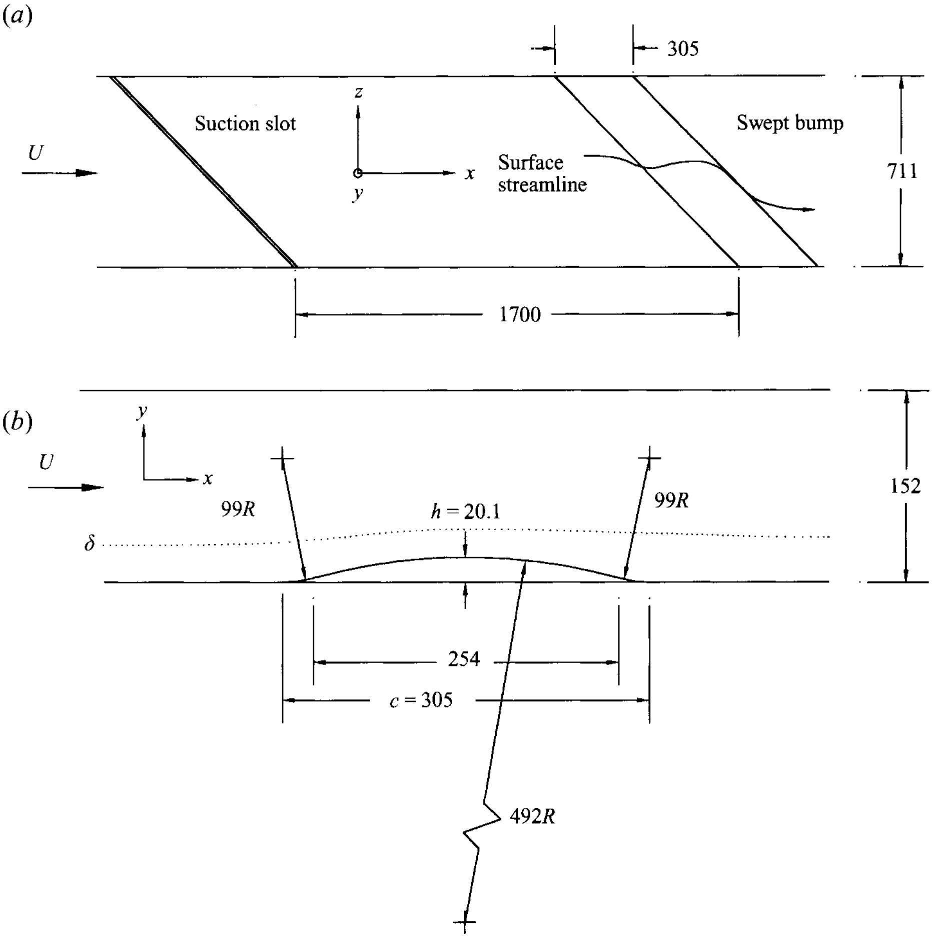

FIGURE 1. (*a*) Top view of the test section. (*b*) Side view of the bump profile. Dimensions in millimetres.

bump mounted on a cylinder. The flow was along the length of the cylinder so the boundary layer developed for varying lengths before encountering the bump. The boundary-layer thickness to bump height ratio (δ/h) ranged from 0.4 to 0.9 and the boundary-layer thickness to convex radius of curvature (δ/R) varied from 0.01 to 0.03. The results presented were very limited, but did show a significant reduction in A_1 as in previous three-dimensional turbulent-boundary-layer experiments.

The objective of this paper is to report the turbulence characteristics of a boundary layer over a swept bump and to compare them to the two-dimensional bump results. The results will contribute to the existing knowledge about three-dimensional turbulent boundary layers and will provide new insight into the complex combination of streamwise pressure gradient, longitudinal surface curvature, and mean flow three-dimensionality. The mean velocity and turbulent stress profiles will be presented at several locations above and downstream of the swept bump. Of particular interest will be the effect on the vertical turbulent mixing and the relative alignment of shear stress and strain rate vectors.

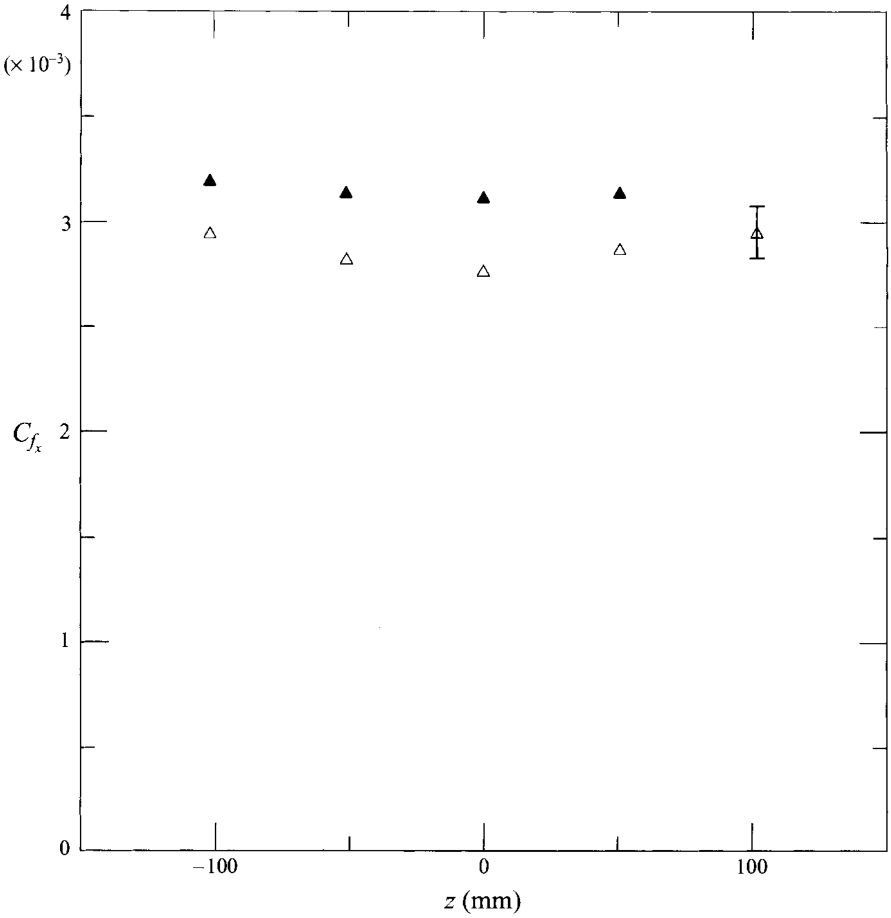

FIGURE 2. Spanwise profiles of the skin friction coefficient, x-component, at ▲, $x' = -0.5$ and △, $x' = 1.17$.

2. Facility and experimental techniques

The experiments were performed in a low-speed blower-driven wind tunnel with a 152 mm × 711 mm rectangular test section as sketched in figure 1(*a*). All data reported in this paper correspond to a nominal velocity of 17.7 m s^{-1} and a free-stream turbulence intensity of 0.2% at the first measurement location. Measurements were performed on the tunnel floor which had a suction slot swept at 45° to create a new boundary-layer origin. The boundary layer was tripped 150 mm downstream of the suction slot and developed for 1.7 m upstream of the bump. Figure 1(*b*) shows the cross-section shape of the bump, which was identical to the two-dimensional bump described in Webster *et al.* (1996). The solid aluminium bump model was bolted to the tunnel floor. In both experiments the initial momentum-thickness Reynolds number was approximately 3800, the initial boundary-layer thickness to bump height ratio (δ/h) was 1.5, and the boundary-layer thickness to convex radius of curvature (δ/R) was 0.06.

All measurements are reported in the tunnel coordinate system, such that x, y and z are the free-stream, wall normal, and spanwise directions, respectively. The streamwise coordinate, $x' = (x-x_0)/c$, is normalized by the bump chord length, making zero the bump leading edge, 0.5 the apex, and 1.0 the trailing edge. The origin for the y-coordinate is the tunnel floor or the bump surface for locations over the

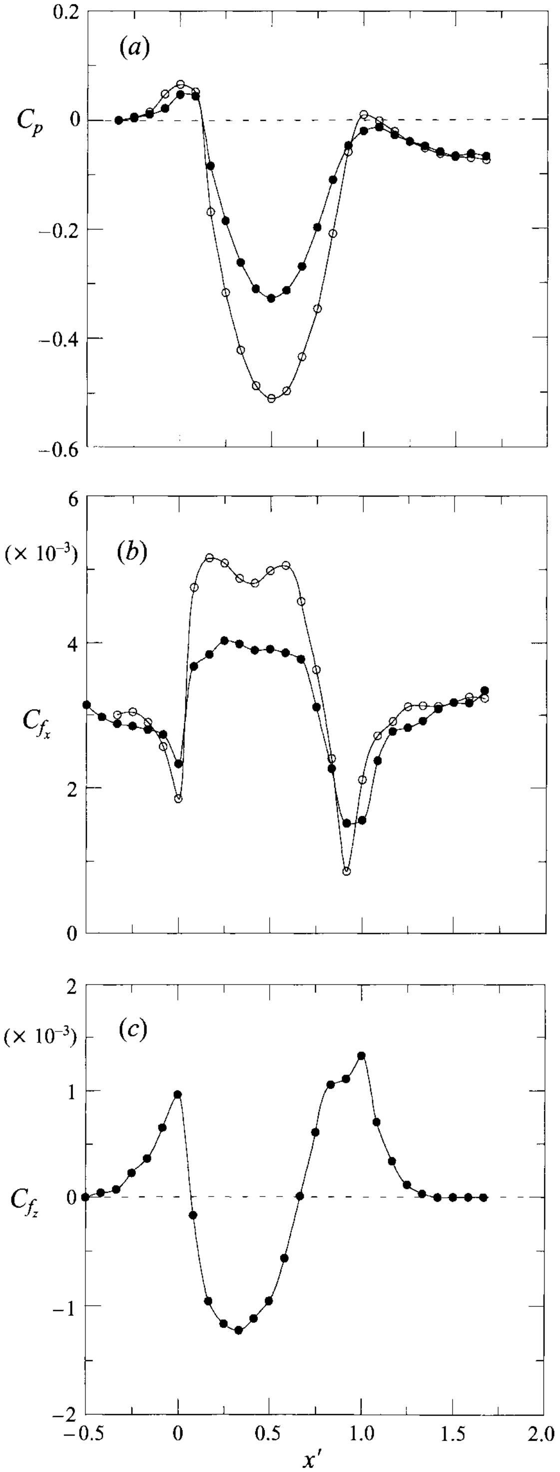

FIGURE 3. (*a*) Static pressure coefficient. (*b*) Skin friction coefficient, x-component. (*c*) Skin friction coefficient, z-component. Swept bump data shown with solid symbols and two-dimensional bump data shown with open symbols.

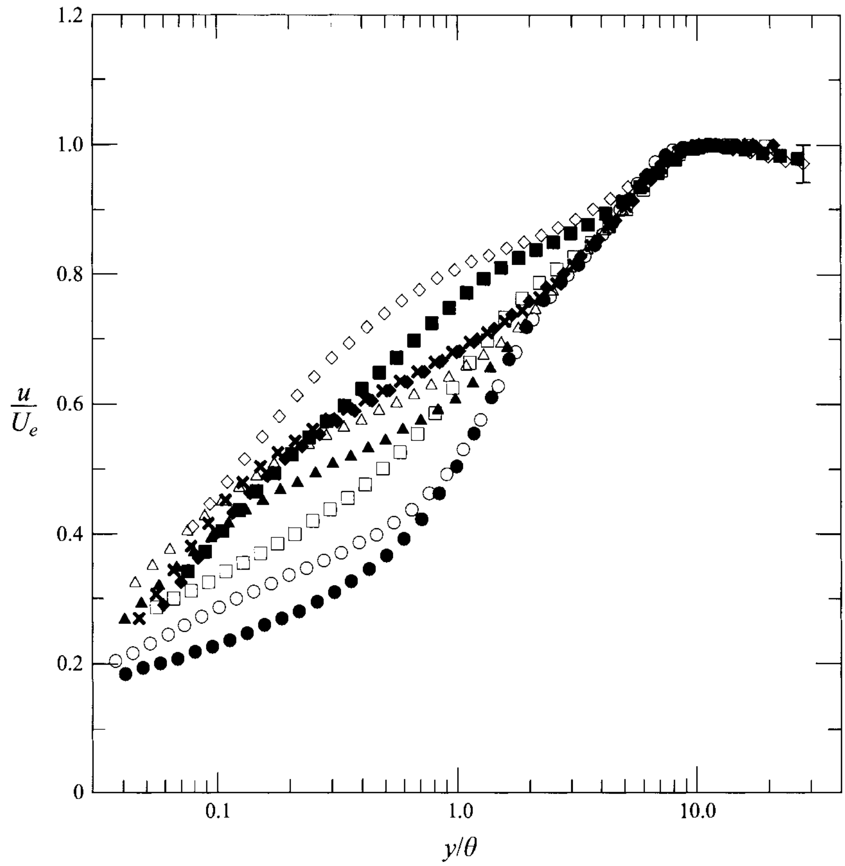

FIGURE 4. Mean u-velocity profiles; ◆, $x' = -0.5$; ◇, 0.5; ■, 0.67; □, 0.83; ●, 0.92; ○, 1.0; ▲, 1.16; △, 1.33; ×, 1.67.

x'	U_e (m s^{-1})	δ^* (mm)	θ (mm)	H	Re_θ	Symbol
−0.50	17.7	4.63	3.36	1.39	3810	◆
0.50	19.6	3.06	2.53	1.21	3140	◇
0.67	19.4	3.39	2.66	1.28	3280	■
0.83	18.8	5.24	3.60	1.45	4370	□
0.92	18.4	8.05	4.82	1.67	5590	●
1.00	18.3	8.65	5.53	1.62	6140	○
1.17	18.2	7.07	4.89	1.44	5610	▲
1.33	18.3	6.16	4.41	1.40	5230	△
1.50	18.3	5.88	4.27	1.38	5000	★
1.67	18.3	5.82	4.25	1.37	4950	×

TABLE 1. Integral parameters at profile locations.

bump. The y-axis is maintained normal to the tunnel floor even at locations above the bump because the initial boundary-layer thickness was greater than the bump height.

The purpose of the swept suction slot was to start the boundary-layer growth at a uniform distance from the bump to produce uniform conditions along the span of the bump. The same technique was employed by Bradshaw & Pontikos (1985) to simulate the 'infinite' swept wing. This allowed all the measurements to be taken along the tunnel centreline. Figure 2 shows the spanwise variation of the skin friction coefficient

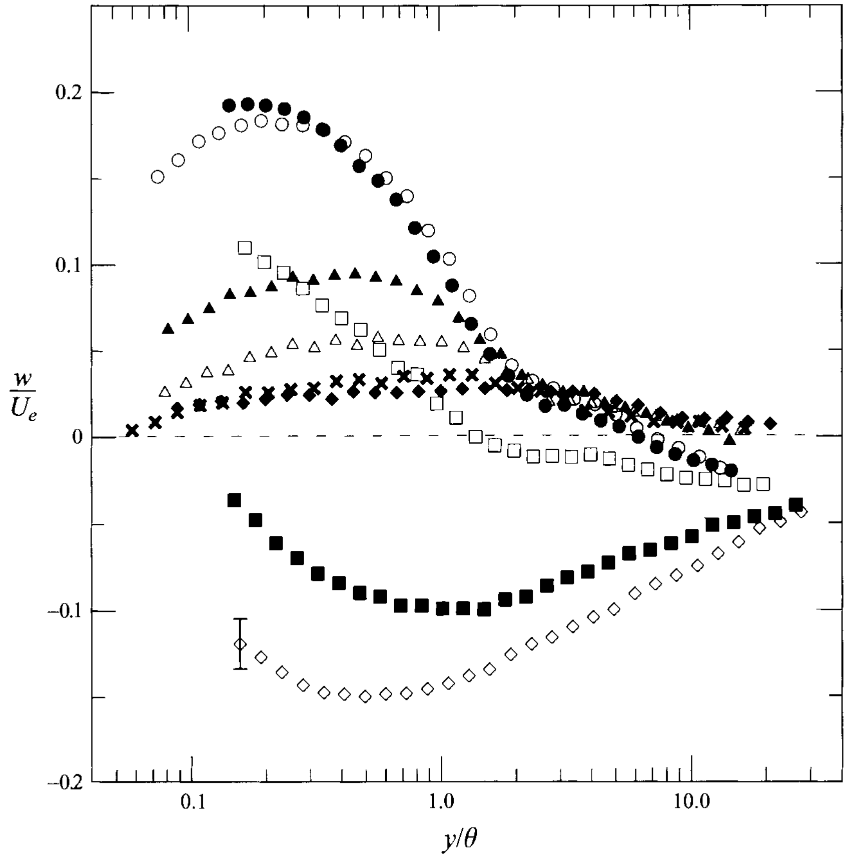

FIGURE 5. Mean w-velocity profiles. Symbols as in figure 4.

upstream and downstream of the bump. The figure shows that there were only small variations across the middle third of the tunnel. The mean velocity and turbulent stress profiles were similarly uniform in the spanwise direction. Surface-oil flow visualization showed excellent spanwise uniformity, corroborating the quantitative results.

Wall static pressure data were measured through 0.635 mm diameter surface pressure taps using a Setra differential pressure transducer (model 239, ± 2.5 in. H_2O range). The surface flow direction was measured from dye streaks produced using the oil of wintergreen and ink flow visualization technique described by Langston & Boyle (1982). The magnitude of the wall skin friction was measured with an oil flow fringe imaging technique (Monson, Mateer & Menter 1993) that relies on the proportionality of the oil film thickness to the wall shear. An in-tunnel calibration station was located upstream of the bump at location $x' = -0.5$ where the skin friction could be deduced from the law of the wall. The fringe spacing was measured along the direction previously determined with the surface flow visualization, and then projected into x- and z-components. Fifteen independent measurements were collected at each streamwise location and averaged. The measurements showed good repeatability and the uncertainty was estimated to be $\pm 5\%$ of the reference value.

The velocity measurements were performed with the single-wire and cross-wire probes described in Littell & Eaton (1994). The probes used 2.5 μm platinum-coated tungsten wire which was copper plated and then etched for an active length to diameter ratio of 250. This gave an active length of $l^+ = 30$ at the location $x' = -0.5$. The cross-

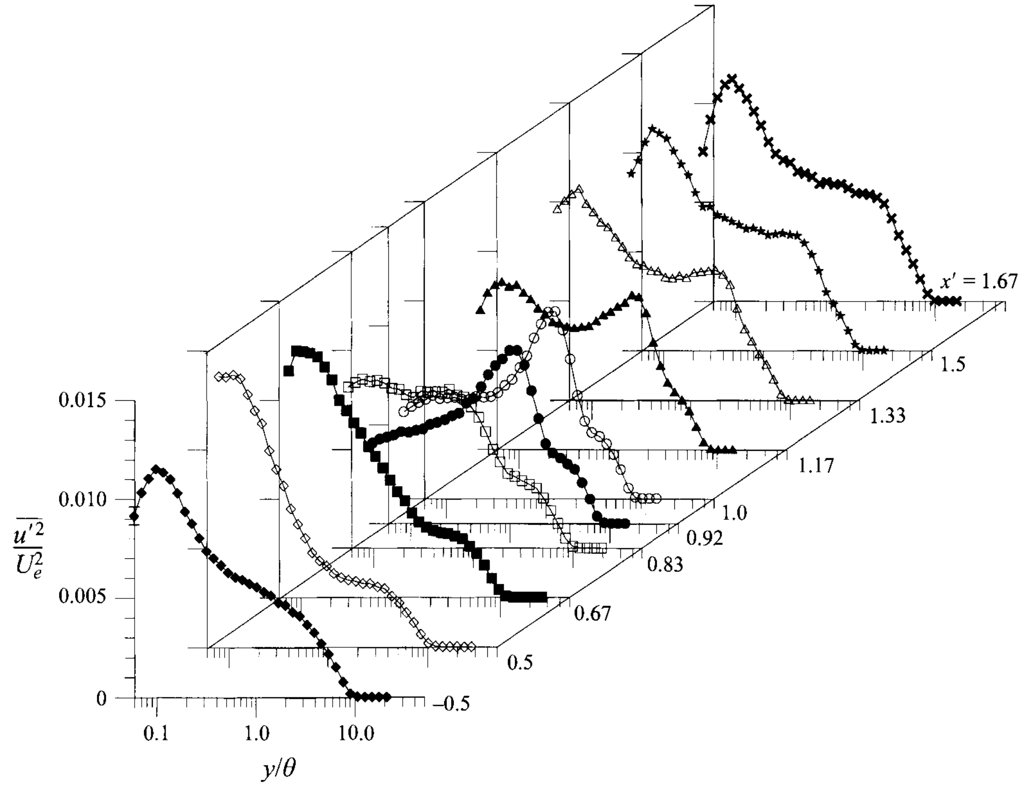

FIGURE 6. Profiles of $\overline{u'^2}$; ◆, $x' = -0.5$; ◇, 0.5; ■, 0.67; □, 0.83; ●, 0.92; ○, 1.0; ▲, 1.16; △, 1.33; ★, 1.5; ×, 1.67.

wires were separated by 0.35 mm and could be rotated about their axes in 45° increments allowing for measurements of all six Reynolds stresses. The data were measured with a TSI constant temperature anemometer (model IFA-100) operating at a resistance ratio of 1.8. The voltage signal was d.c. shifted and amplified and then filtered at 10 kHz. At each location 5000 samples were collected at 250 Hz. The cross-wire probe was aligned with the mean velocity vector at every measurement point in order to minimize the uncertainty. The probe was calibrated in the tunnel and the results were fitted to King's law with a variable exponent. The air temperature was measured before data acquisition at every point, and the Bearman (1971) temperature correction was applied to the measured hot-wire voltage. The effective wire angles were found by assuming a cosine response and following the calibration yawing procedure described in Westphal & Mehta (1984).

The probes were positioned using a two-axis traverse which had an accuracy of 0.0015 mm and 0.003 mm in the vertical and streamwise directions, respectively. The initial vertical position of the probes was set by observing the electrical contact resistance between the probe prongs (an attached post was used for the cross-wire probe) and the conducting floor of the test section. The data acquisition was performed with a 486 PC clone and National Instruments AT-MIO-16 and GPIB-PCII boards. An external simultaneous sample and hold circuit was used to collect the cross-wire voltages.

Following the analysis of Anderson & Eaton (1989) of the theoretical hot-wire probe operation, the following uncertainties were conservatively estimated for the hot-wire measurements. The mean velocities had an uncertainty of ±3% of the local

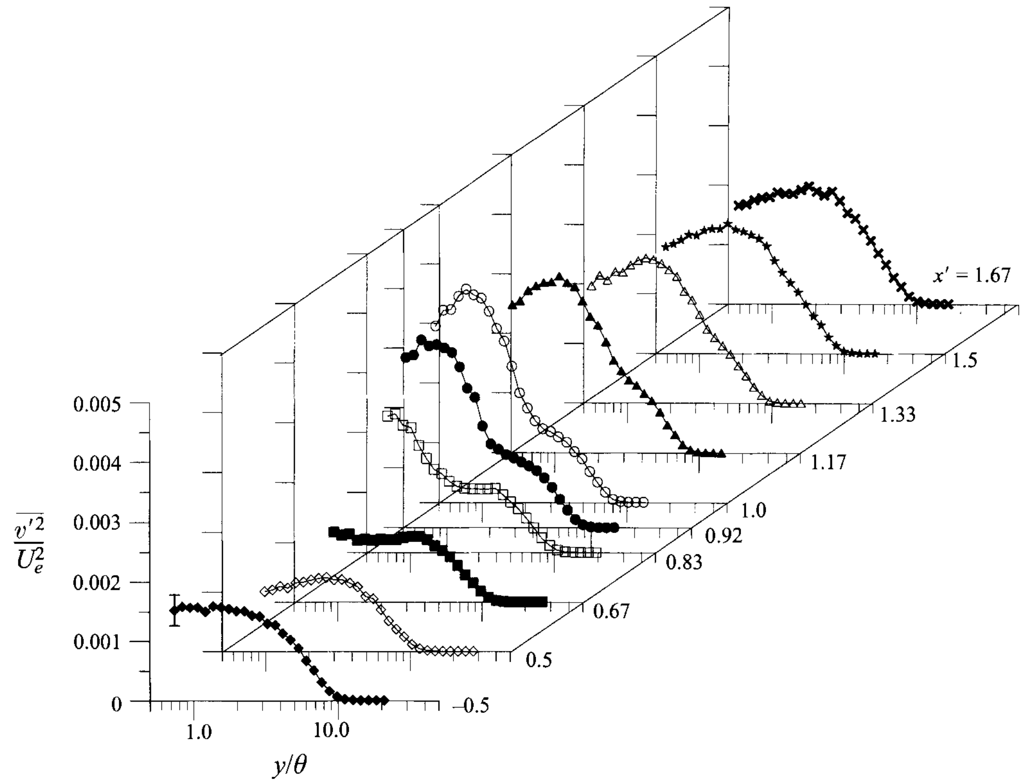

FIGURE 7. Profiles of $\overline{v'^2}$. Symbols as in figure 6.

streamwise velocity. The normal Reynolds stress components had an uncertainty of $\pm 5\%$ of the local value of $\overline{u'^2}$. The shear stress components had an uncertainty of $\pm 10\%$ of the local value of $\overline{u'v'}$. Sample error bars are shown on the mean velocity and Reynolds stress profiles. Typically, the repeatability and agreement between the single wire and cross-wire measurements was better than the theoretically estimated uncertainty ($\pm 1\%$ for the mean velocity components and $\pm 3\%$ for the Reynolds stress quantities).

3. Experimental results

Figure 3(*a*) shows the static pressure coefficient, $C_p = (P_{static} - P_{ref})/\frac{1}{2}\rho U_{ref}^2$, as a function streamwise location, with the reference location at $x' = -0.33$. The flow experienced a mild adverse pressure gradient just upstream of the bump. Over the bump, the streamwise pressure gradient was strongly favourable followed by strongly adverse. Downstream of the bump the pressure gradient was mildly favourable. The pressure on the two-dimensional bump showed the same qualitative nature, but the variations were larger. The difference was due to two effects. First, the swept bump caused slightly less flow blockage at a given cross-section and therefore caused less acceleration and subsequent deceleration of the free stream. Secondly, the turning of the flow near the wall in the swept case increased the radii of curvature of the flow streamlines, thereby reducing curvature-induced pressure variations.

The *x*-component of the skin friction coefficient, $C_{f_x} = (\tau_w)_x/\frac{1}{2}\rho U_{ref}^2$, is shown in figure 3(*b*). The skin friction generally corresponded to the streamwise pressure gradient, reaching high values in the favourable pressure gradient region and falling

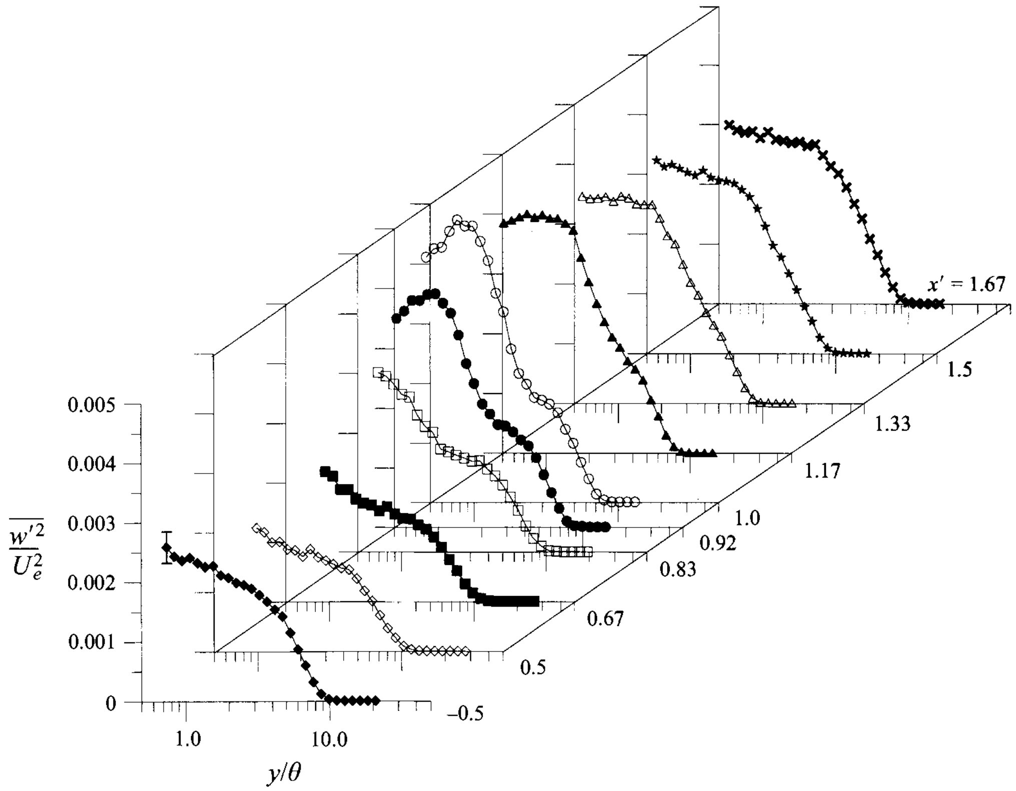

FIGURE 8. Profiles of $\overline{w'^2}$. Symbols as in figure 6.

rapidly in the adverse pressure gradient region. Despite the sharp decrease in skin friction on the downstream side of the bump, measurements and flow visualization confirmed that the flow did not separate. The dip in the two-dimensional curve near the bump apex can be attributed to the early stages of relaminarization. The swept bump data do not show a similar dip, which indicates that the more moderate streamwise pressure gradient was not sufficient to begin the relaminarization of the boundary layer. The acceleration parameter, $\Delta_p = -\nu(\mathrm{d}p/\mathrm{d}x)/\rho u_\tau^3$, reached a maximum value on the upstream side of the bump of 0.019 which barely exceeds the value of 0.018 set by Patel (1965) to denote significant departures from the logarithmic layer. The acceleration parameter had a peak value of 0.025 for the two-dimensional bump.

Figure 3(c) shows the z-component of the skin friction, $C_{f_z} = (\tau_w)_z/\frac{1}{2}\rho U_{ref}^2$. Positive values correspond to surface flow along the sweep, and negative values correspond to flow against the sweep. At the bump trailing edge ($x' = 1.0$), the magnitude of the x- and z-components are similar and the surface streamline attained a maximum angle of 40°.

Hot-wire measurements were performed at the upstream reference location ($x' = -0.5$) and at nine locations between the bump apex ($x' = 0.5$) and downstream of the bump at $x' = 1.67$. Table 1 shows the local external velocity, the displacement thickness, the momentum thickness, the shape factor, and the momentum-thickness Reynolds number. The integral parameters are smallest at the bump apex and largest near the trailing edge, owing to the acceleration and deceleration of the boundary layer over the bump. The profiles of mean velocity and turbulent stresses presented in this paper have been normalized by the local external velocity. This normalization masks

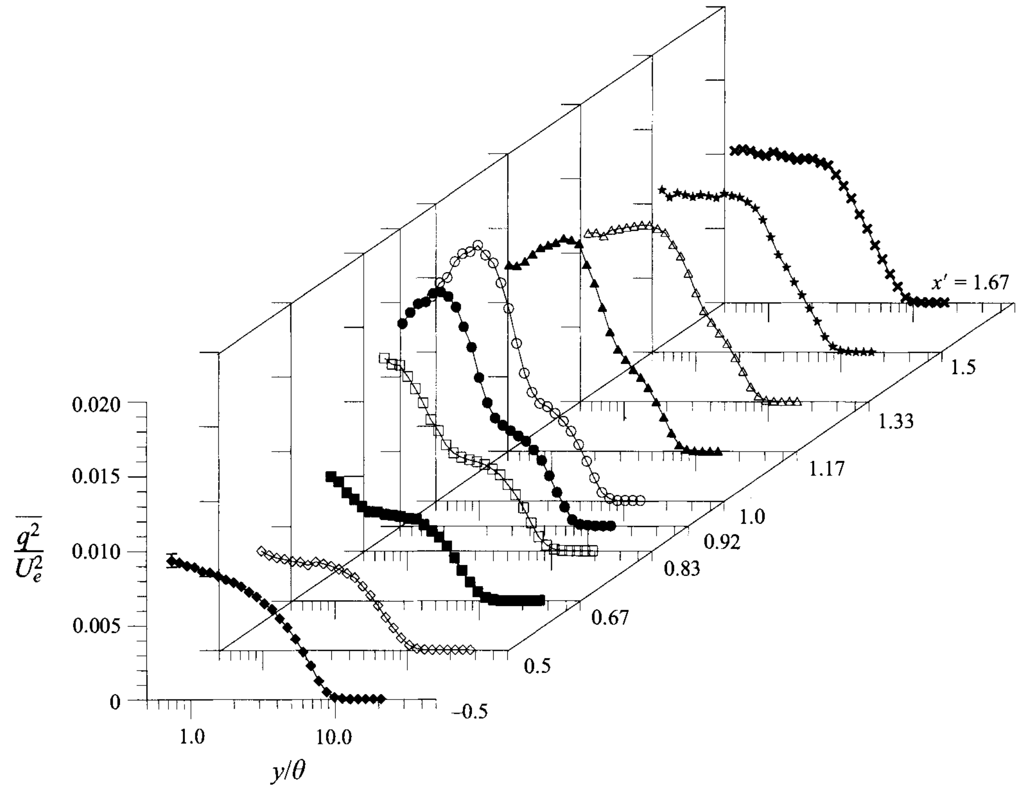

FIGURE 9. Profiles of $\overline{q^2}$. Symbols as in figure 6.

the acceleration but provides ready comparison between profiles at the various locations. The vertical coordinate has similarly been normalized by the local momentum thickness which masks the thinning and growth of the layer, but again provides ready relative comparison between stations. Inner variable scaling has not been employed because of the strong deviation from law of the wall behaviour.

Figures 4 and 5 are the profiles of the u- and w-component mean velocity, plotted in semi-logarithmic coordinates. The v-component mean velocity is not shown here because it was nearly zero except on the downstream side of the bump, where it was small and negative (i.e. the flow was down the bump). The profiles at $x' = -0.5$ showed excellent agreement with the law of the wall.

The profiles above the bump show significant differences from those at the upstream reference location. At the bump apex ($x' = 0.5$) the u-component profile deviated strongly from the log law owing to the favourable pressure gradient on the upstream side of the bump. In some previous three-dimensional turbulent-boundary-layer studies, the velocity magnitude, $(u^2+w^2)^{1/2}$, scaled on inner variables was found to follow the law of the wall, but that was not found in the present case. The w-component mean velocity was strongly negative (i.e. against the sweep) in agreement with the skin friction measurements. Once the flow had crested the bump, the streamwise pressure gradient switched to adverse and the spanwise pressure gradient changed sign. After some lag, the w-component of mean velocity responded to this spanwise pressure gradient change. At $x' = 0.67$ the cross-stream flow through most of the layer was still in the negative direction, although the skin friction component in the z-direction was nearly zero (figure 3(c)). At $x' = 0.83$ the w-component mean velocity was close to zero

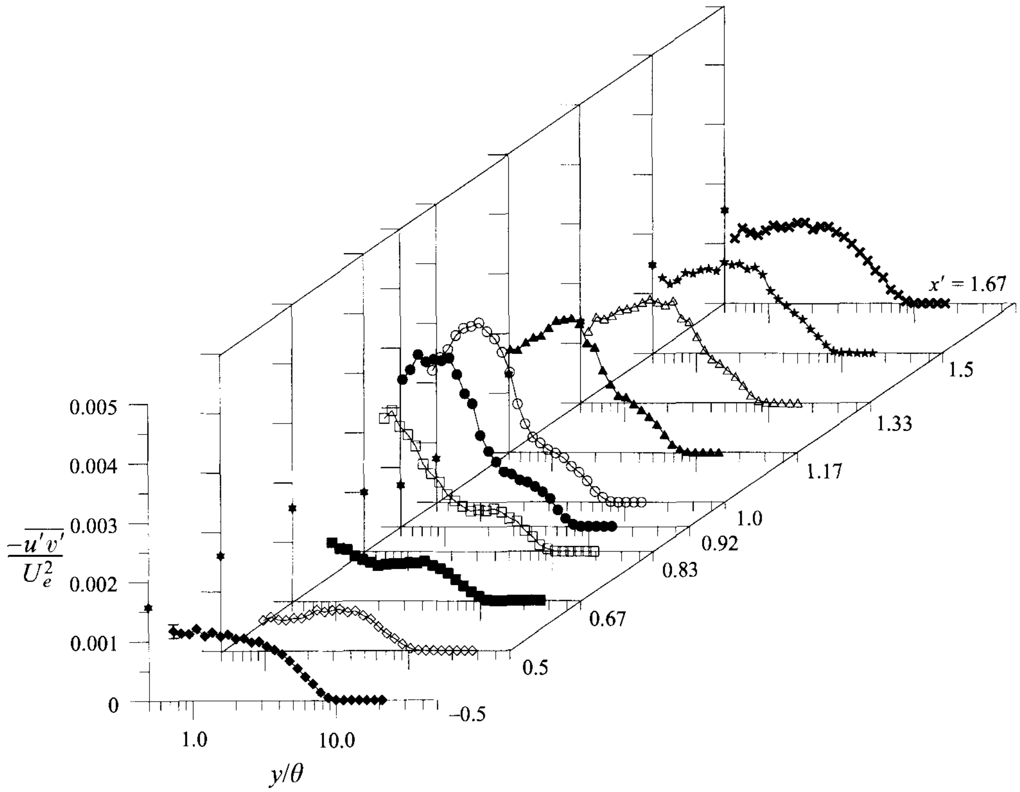

FIGURE 10. Profiles of $\overline{u'v'}$. Symbols as in figure 6. Also shown is $\frac{1}{2}C_{f_x}$, ● (based on local external velocity), on the ordinate.

in the outer part of the layer and positive close to the wall. The cross-stream flow continued to grow positively until the trailing edge, where it had a peak value of nearly $0.2U_e$. The u-component mean velocity grew a large velocity deficit region near the wall, which is typical in adverse pressure gradients.

Downstream of the bump, the flow relaxed back to typical flat-plate boundary-layer behaviour. The u-component mean profiles showed a rapid evolution toward the typical logarithmic layer. At the last measurement location ($x' = 1.67$) the profile nearly agreed with the upstream reference profile. The w-component mean velocity decayed toward zero as the spanwise pressure gradient disappeared. At the last measurement location, the peak spanwise flow was less than $0.03U_e$.

The profiles of the streamwise turbulent normal stress, $\overline{u'^2}$, are shown in figure 6. Since the ten profiles cross each other at several locations, the respective axes have been staggered for clarity. The upstream reference profile agreed well with that measured in previous studies (e.g. Erm & Joubert 1991). The profile at the bump apex ($x' = 0.5$), has a sudden change in slope at approximately $y/\theta = 1$. Baskaran *et al.* (1987) observed the same effect and referred to the change in slope as a knee point. The knee point indicates that the development of a new internal layer had been triggered by the abrupt change in surface curvature at $x' = 0.08$. Outside of the internal layer the normal stress was less than the upstream reference profile, owing to the favourable pressure gradient. On the downstream side of the bump, the internal layer grew away from the wall, as indicated by the outward evolution of the knee point. The peak in the normal stress occurred quite close to the wall at $x' = 0.5$, but moved rapidly outward

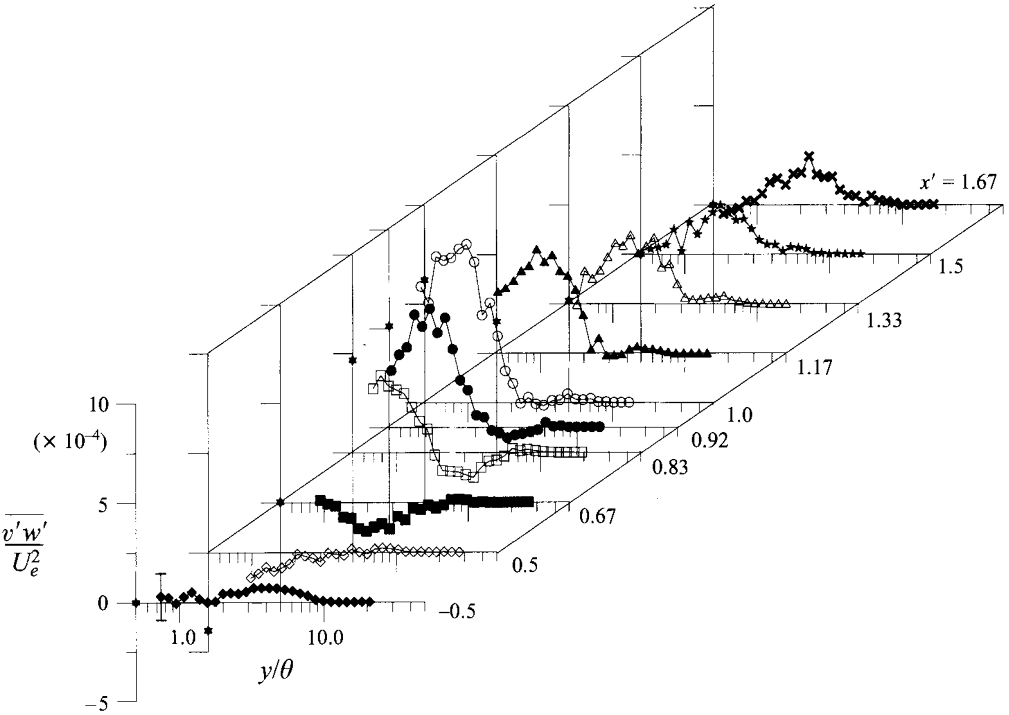

FIGURE 11. Profiles of $\overline{v'w'}$. Symbols as in figure 6. Also shown is $\frac{1}{2}C_{f_z}$, ✱ (based on local external velocity), on the ordinate.

in the strong adverse pressure gradient ($0.5 < x' < 1.0$) owing to rapid boundary-layer growth. This peak decayed downstream of the bump, but its effect was still evident at the last measurement station. A second internal layer was triggered by the abrupt change in surface curvature and rapid reduction in the pressure gradient at $x' = 0.92$. The second internal layer was first observed at $x' = 1.17$ where the profile had double maxima; the inner peak being due to the second internal layer. This inner layer grew through the existing boundary layer leaving the decaying peak in the outer layer unaffected. The evolution of $\overline{u'^2}$ described for the swept bump is qualitatively similar to that observed for the two-dimensional turbulent-boundary-layer analogue including the rapid recovery to the upstream flat-plate boundary-layer behaviour by the last measurement station (6δ downstream of the trailing edge). Detailed comparisons will be made in the following sections.

Figures 7–9 show the profiles of $\overline{v'^2}$, $\overline{w'^2}$ and $\overline{q^2}(=\overline{u'^2}+\overline{v'^2}+\overline{w'^2})$, respectively. It should be noted that the abscissa is different in these figures from that in figure 6 owing to the fact that a cross-wire probe cannot measure as close to the wall as a single-wire probe. The profiles at the upstream reference location again agree well with previous investigations. The normal stresses and turbulent kinetic energy qualitatively follow the same evolution as discussed above for $\overline{u'^2}$. The first internal layer was clearly observed growing from the wall on the downstream side of the bump. The second internal layer was not observed because the cross-wire probe was not close enough to the wall. The profiles downstream of the bump relaxed back to the typical two-dimensional flat-plate shape. The last measured profiles appeared qualitatively similar to the upstream reference profile, although the values are slightly larger in the outer layer.

The $\overline{u'v'}$ shear stress shown in figure 10 also behaved qualitatively like the normal

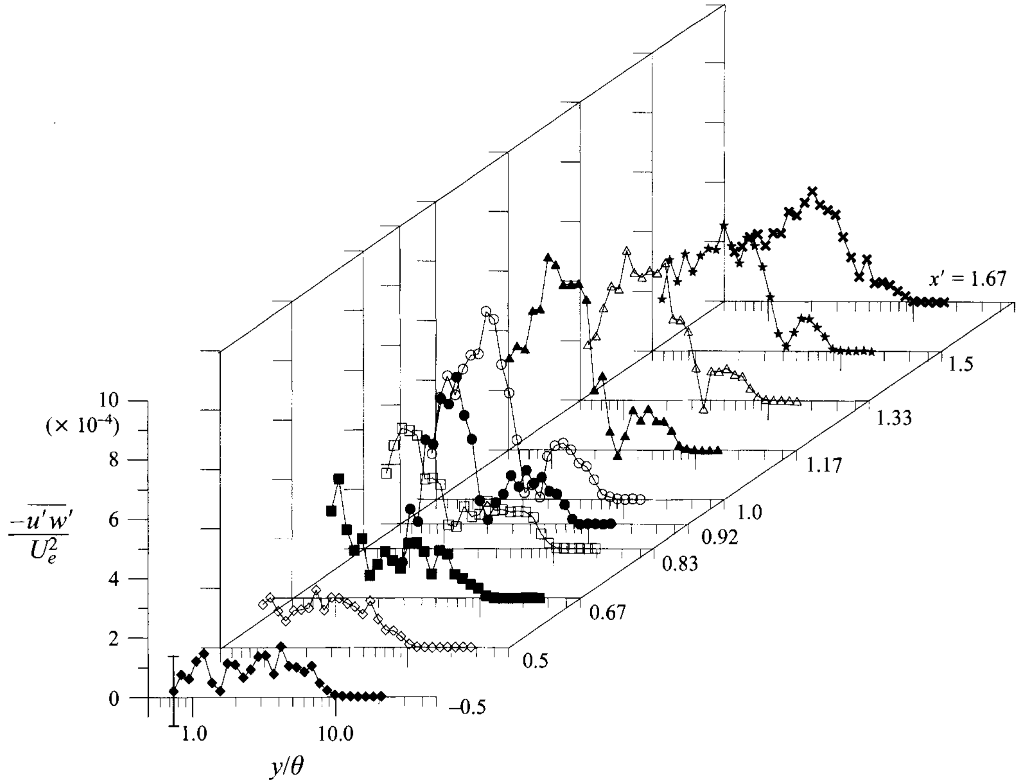

FIGURE 12. Profiles of $\overline{u'w'}$. Symbols as in figure 6.

stresses discussed above. The knee point and local maxima associated with the first internal layer evolved away from the wall beyond $x' = 0.5$. Downstream of the bump, the local maximum of $\overline{u'v'}$ decays rapidly, and the profile at the last station was again very similar to the reference on the upstream flat plate. Also shown on the ordinate for each profile is the x-component skin friction measurement at that x' location. Good agreement is observed between the skin friction measurement and the shear stress profile. The $\overline{v'w'}$ and $\overline{u'w'}$ shear stress profiles are shown in figures 11 and 12. These measurements show more scatter than the previously discussed turbulent stresses because they are considerably smaller quantities. At the upstream reference, $\overline{v'w'}$ was small but non-zero, indicating that the weak turning observed in the mean flow profiles was mildly affecting the shear stress. At the bump apex, $\overline{v'w'}$ was negative across most of the boundary layer. The spanwise flow changed direction on the downstream side of the bump and $\overline{v'w'}$ responded by changing sign. The changes in the shear stress near the wall can be explained simply by examining the production term, $\overline{v'^2}\,\partial w/\partial y$. On the upstream side of the bump $\overline{v'^2}$ was positive and $\partial w/\partial y$ was negative near the wall, hence producing negative $\overline{v'w'}$. On the downstream side of the bump $\partial w/\partial y$ became positive and large near the wall, hence producing large positive $\overline{v'w'}$. The region of negative shear stress moved toward the edge of the boundary layer and decayed. As the cross-stream flow decayed downstream of the bump, $\overline{v'w'}$ decreased owing to the rapid reduction in the production term.

The $\overline{u'w'}$ reference profile was small but non-zero again indicating that the weak cross-flow had a mild effect. The important production terms in the turbulent stress transport equation are $\overline{v'w'}\,\partial u/\partial y$ and $\overline{u'v'}\,\partial w/\partial y$. Both of these terms changed sign

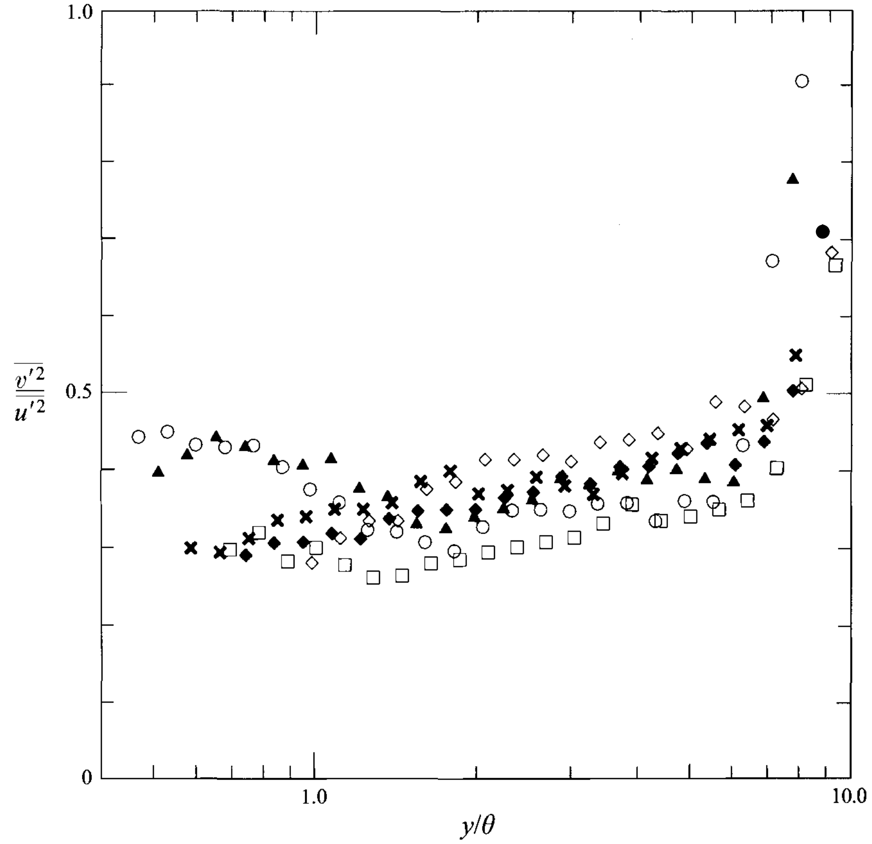

FIGURE 13. Selected profiles of the anisotropy parameter, $\overline{v'^2}/\overline{u'^2}$. Symbols as in figure 6.

from the upstream to the downstream side of the bump. However, $\overline{u'w'}$ remained uniformly negative which indicated that the relative importance of the two terms changed. The local minima observed in the range $1 < y/\theta < 3$ on the downstream side of the bump was a result of the two production terms changing their relative strength. The outer local maximum was a remnant of the production owing to $\overline{u'v'}\,\partial w/\partial y$ on the upstream side of the bump and the inner local maximum was due to the $\overline{v'w'}\,\partial u/\partial y$ term.

4. Reynolds-averaged flow structure

In this section we present several derived quantities that are of interest for Reynolds averaged modelling. Before calculating the derived quantities, the measured profiles were smoothed in the y-direction replacing each data point with a weighted average of itself and its two neighbours. Figure 13 shows the anisotropy parameter, $\overline{v'^2}/\overline{u'^2}$. The values range between 0.3 and 0.4 and showed little variation between profiles. Profiles of $\overline{w'^2}/\overline{u'^2}$ are not shown here but had the same behaviour. As shown in figures 6–8, the normal stresses were affected by the bump, however the anisotropy parameter indicated that they were responding in unison since their ratio remained nearly constant. The same behaviour was observed in the two-dimensional turbulent-boundary-layer analogue indicating that this is not an effect due to three-dimensionality.

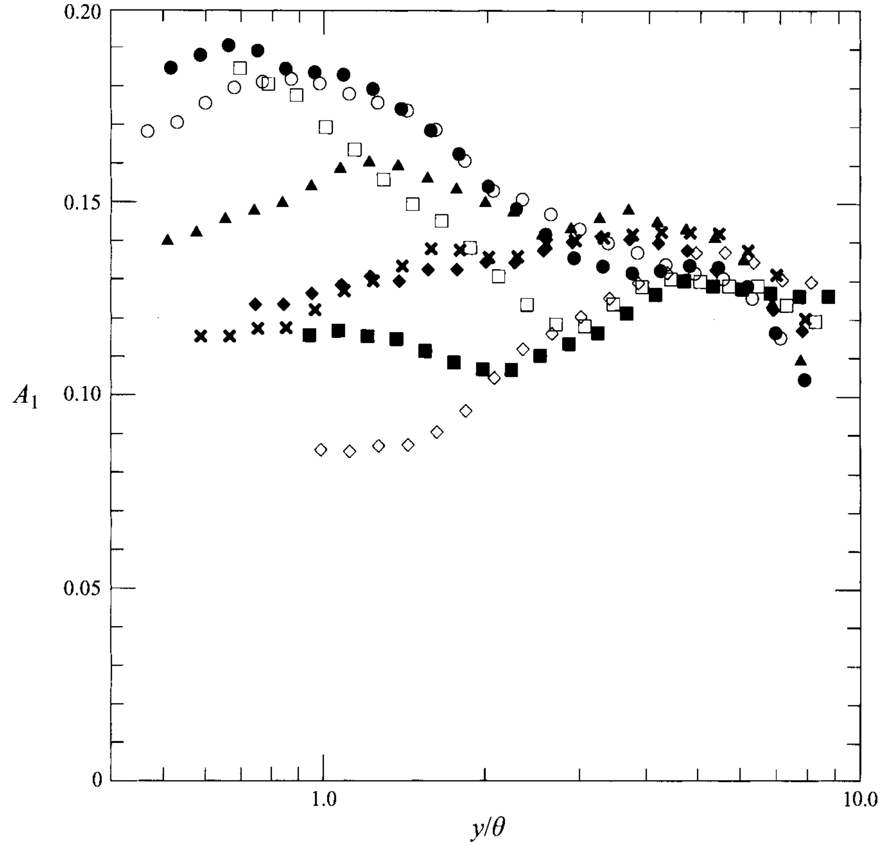

FIGURE 14. Profiles of the Townsend structure parameter, A_1. Symbols as in figure 6.

Profiles of the Townsend structure parameter, $A_1 = (\overline{u'v'}^2 + \overline{v'w'}^2)^{1/2}/\overline{q^2}$ are shown in figure 14. A_1 is independent of rotation around the y-axis and the parameter is generally considered constant across the shear layer in a two-dimensional turbulent boundary layer with a value of approximately 0.15. The upstream reference profile agrees reasonably well with this behaviour, since the profile is nearly flat between 0.13 and 0.14. At the bump apex, A_1 was reduced near the wall to approximately 0.085. In the adverse pressure gradient on the downstream side of the bump, A_1 increased to a maximum of approximately 0.19 near the wall at $x' = 0.92$. Downstream of the bump, A_1 relaxed back to approximately the upstream behaviour. At the last measurement location, A_1 showed slightly depressed values near the wall as compared to the upstream reference profile. The profiles were nearly identical at all locations for y/θ greater than 4 which indicates that the turbulent structure near the edge of the boundary layer was unaffected by the bump. As will be shown in the following section the evolution of A_1 in the flow over the swept bump is nearly identical to that for the two-dimensional turbulent-boundary-layer analogue.

The Prandtl mixing length is not shown but reveals the same trends observed with A_1. Notably, near the bump apex the mixing length was significantly larger than that in a standard flat-plate boundary layer, owing to the favourable streamwise pressure gradient on the upstream side of the bump. Near the bump trailing edge, the mixing length was reduced owing to the adverse pressure gradient. Downstream of the bump, the mixing-length profiles rapidly recovered toward the upstream behaviour.

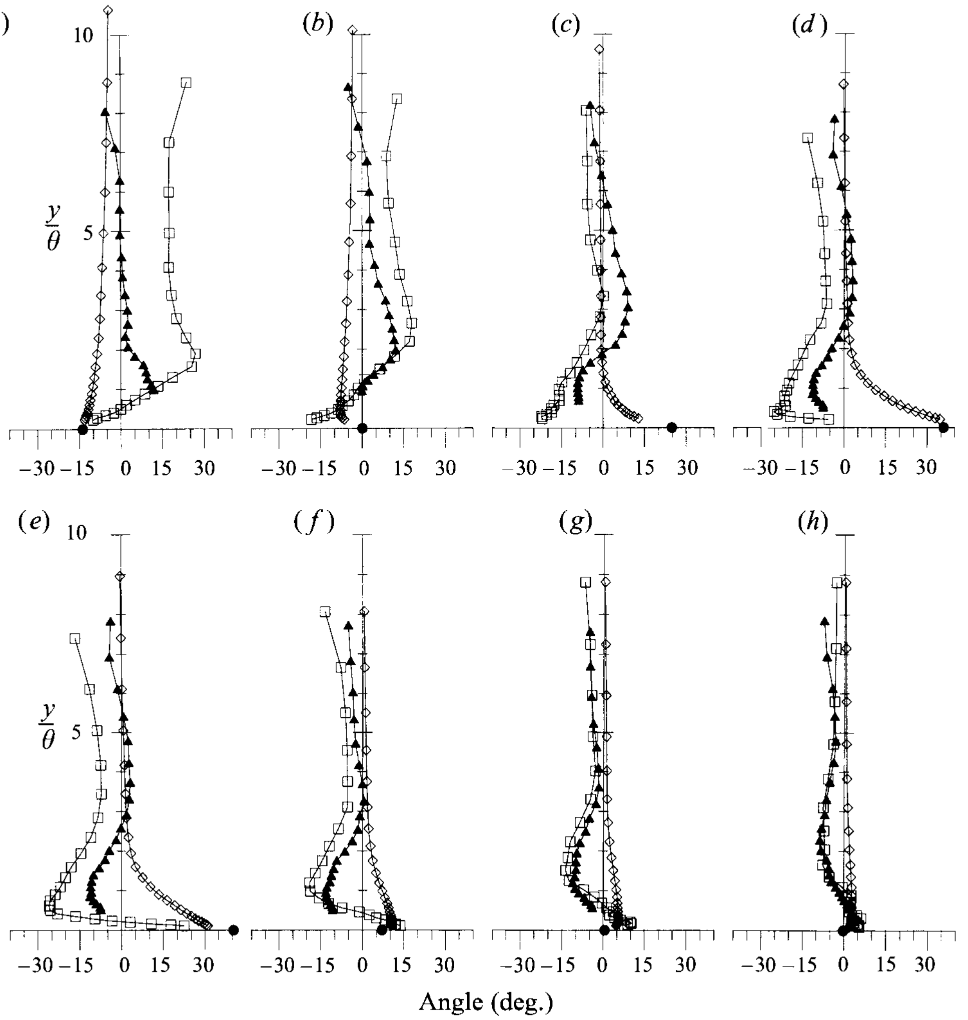

FIGURE 15. Profiles of ◇, the mean flow angle, γ_u; □, the flow gradient angle, γ_g; ▲, the shear-stress angle, γ_τ. Also shown is ●, the wall turning angle at locations: (a) $x' = 0.5$, (b) 0.67, (c) 0.83, (d) 0.92, (e) 1.0, (f) 1.16, (g) 1.33, (h) 1.67.

Figure 15 shows the mean flow angle, $\gamma_u = \arctan(w/u)$, the flow gradient angle, $\gamma_g = \arctan((\partial w/\partial y)/(\partial u/\partial y))$, and the shear stress angle, $\gamma_\tau = \arctan(\overline{v'w'}/\overline{u'v'})$, which illustrate the flow response to the spanwise pressure gradient. Also shown is the wall turning angle measured from the oil of wintergreen flow visualization. The angle was defined as zero along the x-axis and positive in the direction of the sweep (i.e. the sweep angle was +45°). The uncertainty in the angle measurements was ±3° very near the wall and dropped to ±1° in the free stream. The symbol size in the figure corresponds to ±2° which is representative of the stated uncertainty. As expected, the mean flow angle profiles show that the fluid with relatively low momentum near the wall responded first to the spanwise pressure gradient.

Most previous three-dimensional turbulent-boundary-layer studies have found that γ_τ lags γ_g except in cases where the cross-flow switches sign. In the present study, the shear stress lagged the gradient vector at all stations above the swept bump, despite the cross-flow direction reversal. At the bump apex, a moderately strong negative cross-flow had developed with the mean gradient vector considerably larger than the shear

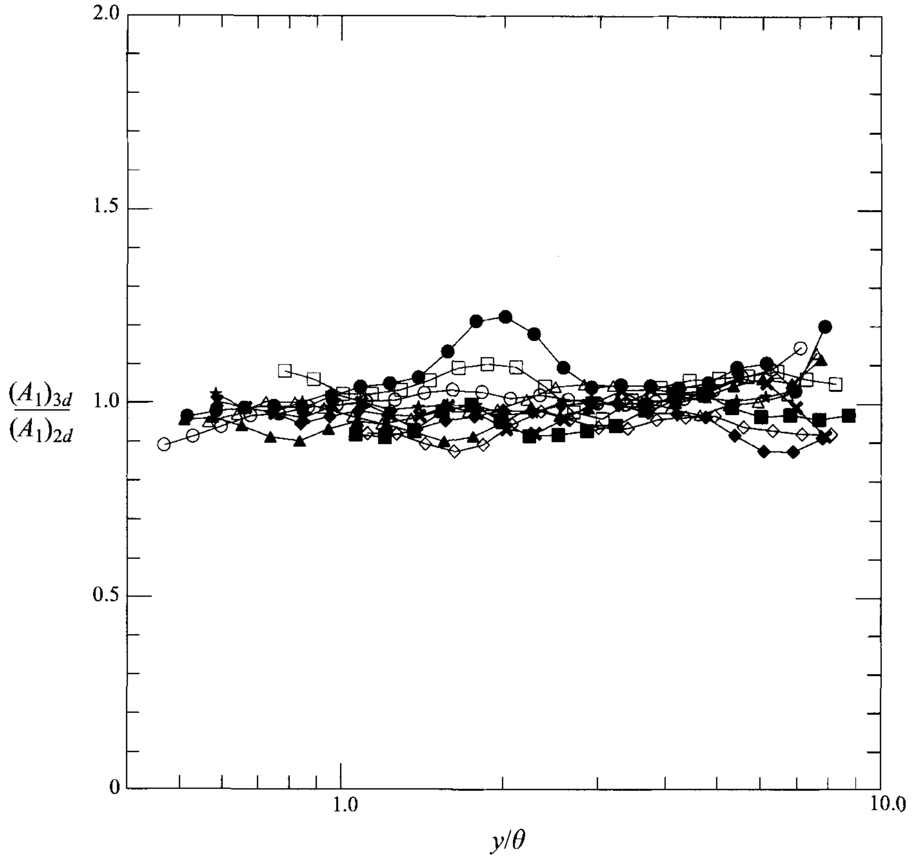

FIGURE 16. Comparison of A_1. Symbols as in figure 6.

stress angle throughout most of the boundary layer (i.e. the shear stress lagged). At $x' = 0.67$ and 0.83, the near-wall flow turned to an increasingly positive angle and the gradient vector became negative through the entire boundary layer. The shear stress vector direction was relatively unchanged in this region. Near the bump trailing edge ($x' = 0.92$ and 1.0) the mean flow angle near the wall was large and positive and the gradient vector angle was large and negative. The shear stress vector started to decrease and again lagged the gradient vector. Downstream of the bump, the mean flow angle and the gradient angle relaxed toward zero. At the last station, the gradient angle had decreased such that it nearly coincided with the shear stress vector. The near alignment of the gradient and shear stress vectors was previously observed by Schwarz & Bradshaw (1994) far downstream of their curved section.

5. Comparison to the two-dimensional bump

The swept bump flow provides the opportunity to examine the combined effects of wall curvature, streamwise pressure gradient and mean cross-flow, but separating these effects is very difficult. In this section, we will discuss the differences between the flow over the swept bump and the flow over the two-dimensional bump described by Webster *et al.* (1996). The reference momentum-thickness Reynolds number was 3800 for both experiments, and the bump profile shape in the (x,y)-plane was identical.

Previous investigations of three-dimensional turbulent boundary layers have found a reduction of A_1 of approximately 20–50%. Figure 16 shows that the Townsend

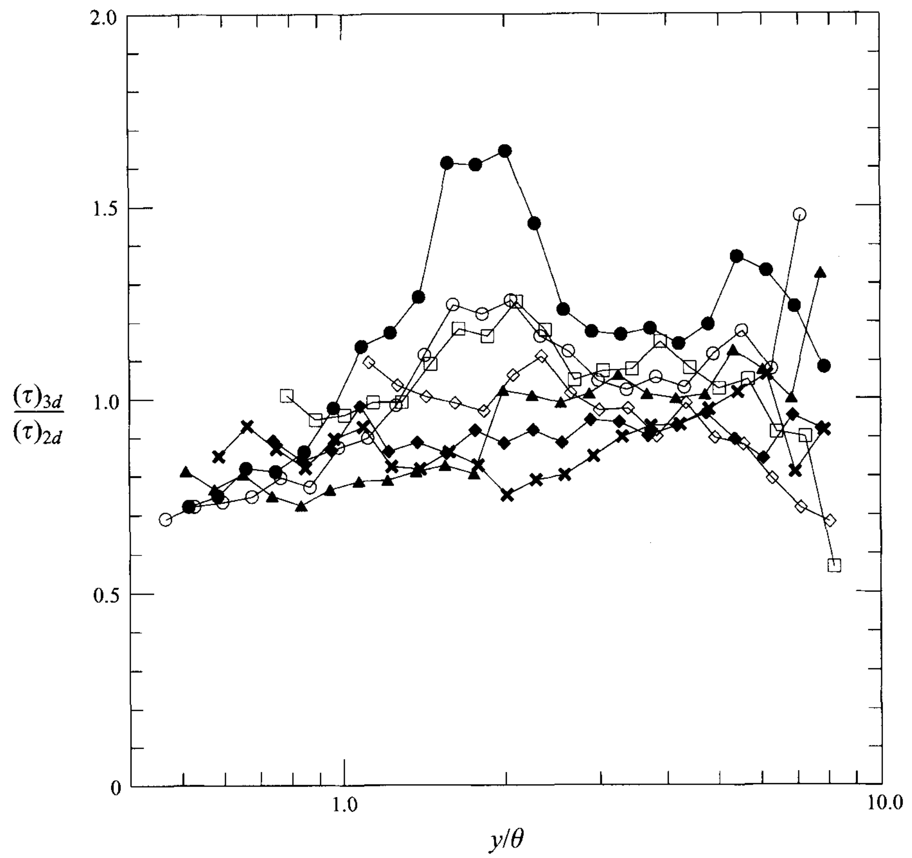

FIGURE 17. Comparison of selected τ profiles. Symbols as in figure 6.

structure parameter of the swept bump flow divided by that from the two-dimensional bump flow was nearly equal to unity, although the profile at $x' = 0.92$ showed an increase of approximately 20%. Hence, the vertical mixing in the boundary layer was not suppressed relative to the turbulent kinetic energy owing to the addition of mean cross-flow. This is remarkable since the structure parameter varied significantly over the bump, and the turbulent shear stress and kinetic energy varied significantly between the swept and two-dimensional cases. This result is also in contrast to most previous three-dimensional turbulent-boundary-layer studies, which show a significant reduction in the vertical mixing relative to the turbulent kinetic energy. Although some previous three-dimensional turbulent-boundary-layer studies had difficulty separating the effects due to streamwise pressure gradients, it seems unlikely that every study is erroneous. A more likely explanation is that the effect of the strong streamwise pressure gradient dominates the modification of the structure parameter in the current flow. The addition of cross-flow on a severely perturbed boundary layer may not have a significant additional influence.

The turbulent shear stress and kinetic energy were individually affected by the mean cross-flow. Figures 17 and 18 compare the turbulent shear stress, $\tau = (\overline{u'v'}^2 + \overline{v'w'}^2)^{1/2}$, and $\overline{q^2}$, respectively. These ratios show significant differences between the swept and two-dimensional bumps. For both quantities, the upstream reference profile ratios were nearly unity, indicating the turbulent characteristics of the approaching flat-plate boundary layer were similar. Above the bump, both the ratios exceed unity because the

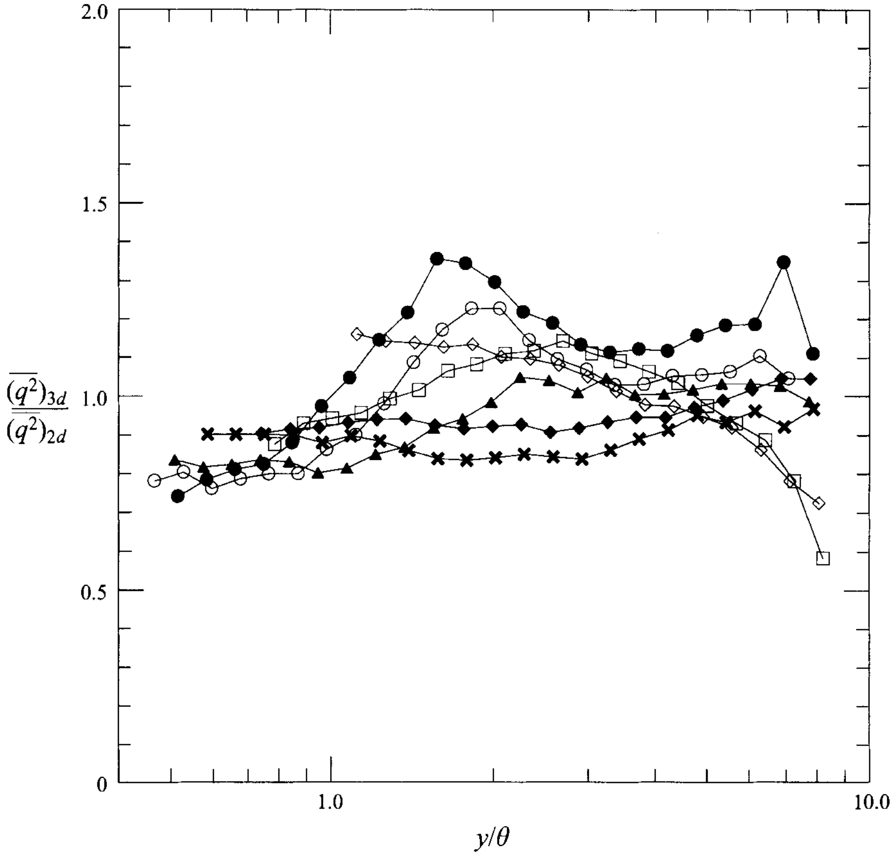

FIGURE 18. Comparison of selected $\overline{q^2}$ profiles. Symbols as in figure 6.

acceleration on the upstream side of the bump was less severe in the swept case, so the turbulent fluctuations were not suppressed as much. Downstream of the bump, the ratio of both quantities is less than unity because the adverse pressure gradient was similarly less severe in the swept case. Despite the variation of these quantities, their ratio remains nearly constant, as observed in figure 16.

6. Conclusions

The experimental results from the complex flow over a swept bump have been presented and discussed. The resulting turbulent boundary layer was influenced by alternating signs of streamwise pressure gradient, wall curvature and mean cross-flow. An internal layer was triggered by the discontinuity in wall curvature at $x' = 0.08$. The internal layer grew away from the wall in the adverse pressure gradient on the downstream side of the bump. A second internal layer was triggered by the surface curvature discontinuity at $x' = 0.92$. The flow downstream of the bump relaxed quickly and at the last measurement station, $x' = 1.67$, the boundary layer strongly resembled the upstream flat-plate reference flow. This was the same qualitative behaviour observed with the two-dimensional bump.

The streamwise pressure gradient in the swept bump case was attenuated relative to the two-dimensional bump because the swept bump created less blockage to the flow and the radii of curvature of the near wall streamlines was larger. The skin friction variation generally followed the streamwise pressure gradient and was similarly attenuated relative to the two-dimensional bump.

The turbulent stresses varied greatly above and downstream of the bump owing primarily to the growth of the internal layers and the presence of the streamwise pressure gradients. Despite the variation, the profiles of the anisotropy parameters, $\overline{v'^2}/\overline{u'^2}$ and $\overline{w'^2}/\overline{u'^2}$, showed good similarity which indicates that the normal stresses were responding in unison. The profiles of A_1 showed significant deviation from typical flat-plate boundary layer behaviour, which can be explained by the influence of the streamwise pressure gradient. By comparing these to the two-dimensional bump flow at the same Reynolds number, it was clear that the vertical mixing relative to the turbulent kinetic energy was not significantly influenced by the addition of mean cross-flow to this already complex flow. This conclusion is in contrast to previous three-dimensional turbulent-boundary-layer studies which show a reduction in A_1, and may indicate that cross-flow has little additional influence on the structure parameter in a significantly distorted boundary layer.

Another observation of previous three-dimensional turbulent boundary layer investigations is that the turbulent shear stress vector lags the strain rate vector. Despite the flow reversal on the downstream side, this was affirmed by the present experiment.

The data are available in electronic form from the authors. This work was supported by the Office of Naval Research under grant number N0001494-1-0070 monitored by Dr L. P. Purtell. Thanks to Dr D. Driver at NASA-Ames for his helpful demonstration of the oil flow fringe imaging technique. Thanks also to Professor L. Langston for his tips regarding the oil of wintergreen surface flow visualization.

REFERENCES

ANDERSON, S. D. & EATON, J. K. 1989 Reynolds stress development in pressure-driven three-dimensional turbulent boundary layers. *J. Fluid Mech.* **202**, 263.

BASKARAN, V., PONTIKIS, Y. G. & BRADSHAW, P. 1990 Experimental investigation of three-dimensional turbulent boundary layers on 'infinite' swept curved wings. *J. Fluid Mech.* **211**, 95.

BASKARAN, V., SMITS, A. J. & JOUBERT, P. N. 1987 A turbulent flow over a curved hill. Part 1. Growth of an internal boundary layer. *J. Fluid Mech.* **182**, 47.

BEARMAN, P. W. 1971 Corrections for the effect of ambient temperature drift on hot-wire measurements in incompressible flow. *DISA report* 11, p. 25.

BERG, B. VAN DEN, ELSENAAR, A., LINDHOUT, J. P. F. & WESSELING, P. 1975 Measurements in an incompressible three-dimensional turbulent boundary layer, under infinite swept wing conditions, and comparison with theory. *J. Fluid Mech.* **70**, 127.

BRADSHAW, P. & PONTIKOS, N. S. 1985 Measurements in the turbulent boundary layer on an 'infinite' swept wing. *J. Fluid Mech.* **159**, 105.

COLEMAN, G. N., FERZIGER, J. H. & SPALART, P. R. 1990 A numerical study of the turbulent Ekman layer. *J. Fluid Mech.* **213**, 313.

ERM, L. P. & JOUBERT, P. N. 1991 Low-Reynolds-number turbulent boundary layers. *J. Fluid Mech.* **230**, 1.

FERNHOLZ, H. H. & VAGT, J.-D. 1981 Turbulence measurements in an adverse-pressure-gradient three-dimensional turbulent boundary layer along a circular cylinder. *J. Fluid Mech.* **111**, 233.

FLACK, K. A. & JOHNSTON, J. P. 1993 Near-wall investigation of three-dimensional turbulent boundary layers. *Report MD-63*, Mech. Engng Dept, Stanford University.

GILLIS, J. C. & JOHNSTON, J. P. 1983 Turbulent boundary-layer flow and structure on a convex wall and its redevelopment on a flat wall. *J. Fluid Mech.* **135**, 123.

JOHNSTON, J. P. 1970 Measurements in a three-dimensional turbulent boundary layer induced by a swept, forward facing step. *J. Fluid Mech.* **42**, 823.

JOHNSTON, J. P. & FLACK, K. A. 1994 Advances in three-dimensional turbulent boundary layers with emphasis on the wall-layer regions. *Proc. 1994 ASME Fluids Engng Division Summer Meetings*, Part 6 (of 18), FED **184**, 1.

LANGSTON, L. S. & BOYLE, M. T. 1982 A new surface-streamline flow-visualization technique. *J. Fluid Mech.* **125**, 53.

LITTELL, H. S. & EATON, J. K. 1994 Turbulence characteristics of the boundary layer on a rotating disk. *J. Fluid Mech.* **266**, 175.

MONSON, D. J., MATEER, G. G. & MENTER, F. R. 1993 Boundary-layer transition and global skin friction measurement with an oil-fringe imaging technique. *SAE Tech. Paper Series* 932550.

ÖLÇMEN, S. M. & SIMPSON, R. L. 1995 An experimental study of a three-dimensional pressure-driven turbulent boundary layer. *J. Fluid Mech.* **290**, 225.

ÖZCAN, O. 1988 Three component LDA measurements in a turbulent boundary layer. *Exps Fluids* **6**, 327.

PATEL, V. C. 1965 Calibration of the Preston tube and limitations on its use in pressure gradients. *J. Fluid Mech.* **23**, 185.

SCHWARZ, W. R. & BRADSHAW, P. 1994 Turbulent structural changes for a three-dimensional turbulent boundary layer in a 30 degree bend. *J. Fluid Mech.* **272**, 183.

SENDSTAD, O. & MOIN, P. 1992 The near-wall mechanics of three-dimensional turbulent boundary layers. *Report TF-57*, Mech. Engng Dept, Stanford University.

SPALART, P. R. 1988 Direct simulation of a turbulent boundary layer up to $Re_\theta = 1410$. *J. Fluid Mech.* **187**, 61.

TRUONG, T. V. & BRUNET, M. 1992 Test Case T1: Boundary layer in a 'S'-shaped channel, Numerical Simulation of Unsteady Flows and Transition to Turbulence. *Proc. ERCOFTAC Workshop at EPFL, 26–28 March 1990, Lausanne, Switzerland* (ed. O. Pironneau, W. Rodi, I. L. Ryhming, A. M. Savill & T. V. Truong), pp. 78–115, Cambridge University Press.

WEBSTER, D. R., DEGRAAFF, D. B. & EATON, J. K. 1996 Turbulence characteristics of a boundary layer over a two-dimensional bump. *J. Fluid Mech.* **320**, 53.

WESTPHAL, R. V. & MEHTA, R. D. 1984 Crossed hot-wire data acquisition and reduction system. *NASA TM* 85871.